JOURNAL OF COMPUTATIONAL PHYSICS 71, 343–370 (1987)

Comparison of Conservative and Rotational Forms in Large Eddy Simulation of Turbulent Channel Flow

KIYOSI HORIUTI

Institute of Industrial Science, University of Tokyo, 7-22-1, Roppongi, Minato-ku, Tokyo 106, Japan

Received February 10, 1986; revised November 5, 1986

Fully developed turbulent channel flow is studied numerically using large eddy simulation (LES) with a Fourier finite difference method. A prominent feature of this paper lies in the use of a conservative form of the Arakawa type for the convective terms in the Navier–Stokes equations. The results are compared with earlier ones of Moin and Kim [1] based on the rotational form of the convective terms. Noticeable differences are found in quantities such as turbulence intensities, two point correlations, etc. The difference is most prominent in the grid scale portion of the turbulent shear stress. The present results agree well with the recent direct simulation of a mildly curved channel flow by Moser and Moin [2] using the Fourier–Chebyshev polynomial expansions. An estimate is made of the error inherent in the rotational form combined with the second-order central finite difference method. The relationship between the energy production mechanism and helicity is pointed out.

1. INTRODUCTION

Within the last ten years, numerical simulation has become a powerful tool in turbulence research. For full simulation of three dimensional turbulence, however, the number of grid points required is proportional to $Re^{9/4}$, where Re is the Reynolds number. This is greater than the capacity of any existing or envisaged supercomputer. Alternatively, the turbulent eddies may be split into two groups, namely, the large scale (grid scale or GS) eddies and the small scale (subgrid scale or SGS) ones. The former are energetic and dependent on the type of flow. On the other hand, the latter are dissipative and more universal. Therefore, proper SGS models, as well as accurate, efficient, and stable numerical methods for the GS variables, are indispensable for a reliable simulation of high Reynolds number turbulence.

One promising way to fulfill the above requirements is the spectral method combined with large eddy simulation (LES). Fourier expansion is regularly used in the simulation of turbulent channel flow. In this type of flow, the cyclic boundary conditions are compatible with the Navier–Stokes equations in the downstream and

0021-9991/87 $3.00

spanwise directions. In the inhomogeneous direction, finite differences [1, 3, 4] or Chebyshev polynomial expansions [2, 5–7] are used. The Fourier finite difference method is combined with LES in [1 and 4]. On the other hand, the Fourier–Chebyshev polynomial expansion is used in [2, 5–7] without any modeling. In [5–7], attention is focused on the initial stage of transition to turbulence, whereas in [2] fully developed turbulent flows in a mildly curved channel at relatively low Reynolds numbers are simulated.

It is well known that the integral constraints such as the conservation of mean energy are quite important in making computation stable in long-term numerical integrations [8]. Therefore, the conservative form of the Arakawa type [9] or the rotational form [10] is widely used for the convective terms in the Navier–Stokes equations. In the present paper, we refer to the former as the Arakawa form. The rotational form is useful because it preserves mean vorticity, helicity. enstrophy, etc. in addition to mean momentum and energy in the absence of external forces and viscous dissipation. The Arakawa form, however, generally preserves only mean momentum and energy. The rotational form has been successful when combined with Chebyshev polynomial expansions as in [2].

In the present study, a fully developed turbulent channel flow is studied using LES with the Fourier finite difference method. The numerical scheme is basically the same as in [1] and essentially a spectral version of a previous computation [11] in which all partial differential operators were approximated by the finite difference method. The essential points are the choice of the form of the convective terms in the Navier–Stokes equations and the residual stress model [12, 1]. In [1], the rotational form was used. In the present study the Arakawa form is used and the residual stress model is not employed. Comparisons with [1] and the Fourier–Chebyshev computation in [2] are made. Noteworthy differences are found, especially in the balance of the GS portion of turbulent shear stress. It is shown that large truncation errors can occur in the vicinity of the walls when the rotational form is used and the normal derivatives are approximated with the second-order central finite difference method.

2. Governing Equations

We consider an incompressible channel flow whose time evolution is governed by the Navier–Stokes and continuity equations for the velocity components u_i $(i=1, 2, 3)$ and the pressure p:

$$\frac{\partial u_i}{\partial t}+\frac{\partial}{\partial x_j}(u_i u_j)=-\frac{\partial p}{\partial x_i}+\frac{1}{\mathrm{Re}}\nabla^2 u_i+2\delta_{i1}, \tag{1}$$

$$\frac{\partial u_i}{\partial x_i}=0. \tag{2}$$

Here $i, j=1, 2, 3$ correspond to x, y, z, respectively, where x is the downstream

coordinate, y is the spanwise coordinate, z is the normal coordinate, and δ_{ij} is the Kronecker delta symbol. Occasionally, u_i $(i=1, 2, 3)$ are denoted by u, v, w, respectively. The flow is driven by the mean pressure gradient. All variables have been made dimensionless by means of the channel width H and the friction velocity u^* $[=(\tau/\rho_0)^{1/2}$; τ is the wall stress and ρ_0 the density which is assumed constant.]. Re is the Reynolds number defined by u^*H/ν (ν is the kinematic viscosity) and R_c represents the Reynolds number defined in terms of the center-plane velocity U_c and H. Moreover, the horizontal average of a quantity is denoted by angular brackets $\langle \cdot \rangle$, the deviation from the horizontal average by $(\cdot)''$, and the length in wall units by $(\cdot)_+$. The summation convention is used for repeated subscripts.

If f is a function containing all the scales, we define the GS component of f by the convolution of f with a filter function $G_i(x_i, x_i')$ [13]:

$$\bar{f}(x_1, x_2, x_3) = \int_D \prod_{i=1}^{3} G_i(x_i, x_i')\, f(x_1', x_2', x_3')\, dx_1'\, dx_2'\, dx_3'. \tag{3}$$

In the present study, the Gaussian filter is used as G_i $(i=1, 2)$ in homogeneous directions and the top-hat filter is used as G_3 in the z direction. These filters are selected in the same manner as in [1]. Along with this filtering procedure, the velocity field u_i and the pressure p are decomposed into GS and SGS components as

$$u_i = \bar{u}_i + u_i', \qquad p = \bar{p} + p'. \tag{4}$$

Applying the filtering to Eqs. (1) and (2), we get the following filtered momentum and continuity equations:

$$\frac{\partial \bar{u}_i}{\partial t} + \frac{\partial}{\partial x_j}\overline{u_i u_j} = -\frac{\partial \bar{p}}{\partial x_i} + \frac{1}{\mathrm{Re}}\nabla^2 \bar{u}_i + 2\delta_{i1}, \tag{5}$$

$$\frac{\partial \bar{u}_i}{\partial x_i} = 0. \tag{6}$$

Nonlinear terms in Eq. (5) are expressed as follows:

$$\overline{u_i u_j} = \overline{\bar{u}_i \bar{u}_j} + \overline{\bar{u}_i' u_j'} + \overline{u_i' \bar{u}_j'} + \overline{u_i' u_j'}. \tag{7}$$

In this study, the correlations between GS and SGS variables, namely, the second and third terms of (7) are neglected, and the terms with double bars in the x and y directions are explicitly calculated. The Leonard term arising in the z direction [13] is represented by the truncation error of the second-order central finite difference scheme [1].

To proceed further, the SGS Reynolds stress $\overline{u_i' u_j'}$ must be modeled in terms of the filtered variables. We use an eddy viscosity model:

$$\overline{u_i' u_j'} - \frac{1}{3}\delta_{ij}\overline{u_l' u_l'} = -\nu_e\left(\frac{\partial \bar{u}_i}{\partial x_j} + \frac{\partial \bar{u}_j}{\partial x_i}\right), \tag{8}$$

where ν_e is the SGS eddy viscosity. In the present study, the Smagorinsky model [14] is used for ν_e:

$$\nu_e = (c\Delta)^2 \left[\frac{1}{2} e_{ij} e_{ij}\right]^{1/2}, \qquad e_{ij} = \frac{\partial \bar{u}_i}{\partial x_j} + \frac{\partial \bar{u}_j}{\partial x_i}. \tag{9}$$

In these expressions, Δ is the representative grid interval which we take to be $\Delta = (\Delta x\, \Delta y\, \Delta z)^{1/3}$ and Δx, Δy, Δz denote the computational mesh size in the x, y, z directions, respectively. This model may be derived by a statistical approach [15, 16], and c has been chosen equal to 0.1 by computer optimization as in [17]. In order to make (9) compatible with the no-slip boundary condition, Δ is multiplied by the damping function of Van Driest type $1 - \exp(-z_+/A_+)$ with $A_+ = 25$ [18].

In [12 and 1], the eddy viscosity representation (8) is split into two parts, i.e., homogeneous and inhomogeneous parts as

$$\overline{u_i' u_j'} - \tfrac{1}{3}\delta_{ij}\overline{u_l' u_l'} = -\nu_e(e_{ij} - \langle e_{ij}\rangle) - \nu_e^* \langle e_{ij}\rangle, \tag{10}$$

The latter is called the residual stress model. In (10), ν_e is given by (9) with e_{ij} replaced by $e_{ij} - \langle e_{ij}\rangle$. The inhomogeneous eddy viscosity ν_e^* is

$$\nu_e^* = c^*(D\Delta y)^2 \left[\tfrac{1}{2}\langle e_{ij}\rangle\langle e_{ij}\rangle\right]^{1/2}, \tag{11}$$

where c^* was chosen to be 0.065 and D is another damping function [1].

In the present study, the residual stress model is not used for the following reasons; Without the model, the turbulence is sustained. In addition, it is not reasonable that the mean velocity gradient directly comes into the evaluation of the local SGS Reynolds stress. The residual stress model in [1] will be discussed in detail in Section 5.

For later convenience, we give the energy budget for the GS portion of turbulent energy $\langle \bar{u}_i'' \bar{u}_i''\rangle/2$ ($i = 1, 2, 3$, no summation rule):

$$\begin{aligned}\frac{\partial \langle \bar{u}_i''^2\rangle}{\partial t} = {} & -2\delta_{i1}\langle \bar{u}''\bar{w}\rangle \frac{\partial \langle \bar{u}\rangle}{\partial z} - \frac{\partial}{\partial z}\langle \bar{w}\bar{u}_i''^2\rangle \\ & -2\left\langle \left(\nu_e + \frac{1}{\mathrm{Re}}\right)\frac{\partial \bar{u}_i''}{\partial x_j}\frac{\partial \bar{u}_i''}{\partial x_j}\right\rangle - 2\left\langle \bar{u}_i'' \frac{\partial \bar{p}}{\partial x_i}\right\rangle \\ & + \frac{\partial}{\partial z}\left\langle \left(\nu_e + \frac{1}{\mathrm{Re}}\right)\frac{\partial \bar{u}_i''^2}{\partial z}\right\rangle \\ & -2\left\langle \bar{u}_i'' \frac{\partial}{\partial x_j}(\overline{\bar{u}_i\bar{u}_j} - \bar{u}_i\bar{u}_j)\right\rangle. \end{aligned} \tag{12}$$

Similarly, the governing equation for the GS portion of turbulent shear stress is expressed as

$$\frac{\partial\langle\bar{u}''\bar{w}\rangle}{\partial t} = -\langle\bar{w}^2\rangle\frac{\partial\langle\bar{u}\rangle}{\partial z} - \frac{\partial}{\partial z}\langle\bar{u}''\bar{w}^2\rangle$$
$$-2\left\langle\left(\nu_e + \frac{1}{\mathrm{Re}}\right)\frac{\partial\bar{u}''}{\partial x_j}\frac{\partial\bar{w}}{\partial x_j}\right\rangle$$
$$-\left\langle\bar{u}''\frac{\partial\bar{p}}{\partial z} + \bar{w}\frac{\partial\bar{p}}{\partial x}\right\rangle + \frac{\partial}{\partial z}\left\langle\left(\nu_e + \frac{1}{\mathrm{Re}}\right)\frac{\partial\bar{u}''\bar{w}}{\partial z}\right\rangle$$
$$-\left\langle\bar{u}''\frac{\partial}{\partial x_j}(\overline{\bar{u}_3\bar{u}_j} - \bar{u}_3\bar{u}_j) + \bar{w}\frac{\partial}{\partial x_j}(\overline{\bar{u}_1\bar{u}_j} - \bar{u}_1\bar{u}_j)\right\rangle. \tag{13}$$

The terms on the right-hand sides of (12) and (13) are called the GS production, convection, dissipation, velocity-pressure gradient, diffusion, and cascade terms, respectively.

3. Numerical Method

3.1. *Numerical Approximations*

Equation (5) can be recast into the form

$$\frac{\partial\bar{u}_i}{\partial t} + \frac{\partial}{\partial x_j}(\overline{\bar{u}_i\bar{u}_j}) + \frac{\partial\bar{p}}{\partial x_i} - \left(\frac{\partial\langle\nu_e\rangle}{\partial x_j}\right)\left(\frac{\partial\bar{u}_i}{\partial x_j} + \frac{\partial\bar{u}_j}{\partial x_i}\right)$$
$$-\frac{\partial}{\partial x_j}\left[\nu_e''\left(\frac{\partial\bar{u}_i}{\partial x_j} + \frac{\partial\bar{u}_j}{\partial x_i}\right)\right] - 2\delta_{i1} = \left(\langle\nu_e\rangle + \frac{1}{\mathrm{Re}}\right)\nabla^2\bar{u}_i, \tag{14}$$

where the horizontally averaged part of the turbulent viscous terms and its deviation have been separated. The spatial derivatives in the x and y directions are treated by the Fourier spectral method. NX, NY denote the numbers of grid points in the x, y directions, respectively. The z coordinate is stretched using

$$z_k = \tfrac{1}{2}(\tanh(c_0\xi_k)/\alpha + 1)\ (k = 0, NZ-1), \tag{15}$$

where z_k is the coordinate of the kth grid point in the z direction, $c_0 = \log((1+\alpha)/(1-\alpha))/2$, $\xi_k = -1 + 2k\,\Delta\xi$ and $\Delta\xi = 1/(NZ-1)$. The stretching parameter α is 0.98346 as in [1]. For discretizing (14) in time, the terms on the right-hand side are approximated by the Crank–Nicolson scheme while the second-order Adams–Bashforth scheme is used for the remaining terms. As stated in Section 1, an essential point of the present study is the choice of approximation for the convective terms in the Navier–Stokes equations. For the Arakawa form of the equations, a regular mesh system is adopted, and all velocity components and pressure are defined at grid points z_k, as given by (15), and both the momentum and continuity equations are enforced at grid points. This grid system leads to temporal and

spatial oscillation of $\bar{p}$ and led Moin and Kim [1] to adopt a staggered grid system. Their mesh system is staggered only in the z direction; the velocity is defined at z_k and the pressure is at $(z_k+z_{k+1})/2$. The momentum and continuity equations are enforced on different control volumes. In the present study, the Adams–Bashforth method is applied to the pressure gradient terms to avoid oscillations in $\bar{p}$. Thus, we get linear coupled equations for $\bar{u}_i^{n+1}$ and $\bar{p}^n$ as

$$\left(\langle \nu_e \rangle^n + \frac{1}{\mathrm{Re}}\right)\nabla^2 \bar{u}_i^{n+1} - 2\frac{\bar{u}_i^{n+1}}{\Delta t} - 3\frac{\partial \bar{p}^n}{\partial x_i}$$

$$= -\left(\langle \nu_e \rangle^n + \frac{1}{\mathrm{Re}}\right)\nabla^2 \bar{u}_i^n - 2\frac{\bar{u}_i^n}{\Delta t} - \frac{\partial \bar{p}^{n-1}}{\partial x_i} + d_i, \tag{16}$$

$$\frac{\partial \bar{u}_i^{n+1}}{\partial x_i} = 0, \tag{17}$$

where superscript n denotes the time step and d_i contains the remaining terms. To avoid iteration, $\langle \nu_e \rangle$ is evaluated at the nth time step. Consequenlty, Eqs. (16) and (17) are solved as a system of coupled equations as in [1 and 10]. Partial differential operators in the z direction are approximated with second-order central finite differences as

$$\frac{\partial \bar{u}}{\partial z} \sim \frac{\bar{u}_{p,q,k+1} - \bar{u}_{p,q,k-1}}{h_{k+1}+h_k},$$

$$\frac{\partial^2 \bar{u}}{\partial z^2} \sim 2\left(\frac{\bar{u}_{p,q,k-1}}{(h_{k+1}+h_k)h_k} - \frac{\bar{u}_{p,q,k}}{h_{k+1}h_k} + \frac{\bar{u}_{p,q,k+1}}{(h_{k+1}+h_k)h_{k+1}}\right), \tag{18}$$

where $h_k = z_k - z_{k-1}$ and p, q, k are indices of grid positions in the x, y, z directions, respectively.

A system of linear coupled difference equations for each pair of wavenumbers (k'_x, k'_y) is obtained by inserting the Fourier expansion into Eqs. (16) and (17) (Type I);

$$L_k \mathbf{q}_{k-1} + M_k \mathbf{q}_k + U_k \mathbf{q}_{k+1} = \mathbf{g}_k \qquad (k = 1, NZ-2), \tag{19}$$

where L_k, M_k, and U_k are 4×4 matrices, $\mathbf{q}_k = (\tilde{u}_k, \tilde{v}_k, \tilde{w}_k, \tilde{p}_k)^t$ ($(\cdot)^t$ denotes the transpose.) and the right-hand side of (16) and (17) is denoted by $\mathbf{g}_k$ and k'_x, k'_y denote wavenumbers in the x and y directions, respectively. $\tilde{u}_{l,m,k}$ denotes the Fourier transformation of $\bar{u}_{i,j,k}$ and subscripts l, m are omitted here. The coupled system of Eqs. (19) is solved by the conventional method for block tri-diagonal equations.

Here we introduce Type II to elaborate the numerical algorithm. Equations (19) can be rearranged into the form (Type II)

$$A\mathbf{u}^{n+1} + 3B_x\,\mathbf{p}^n = -(A+E)\,\mathbf{u}^n + B_x\,\mathbf{p}^{n-1} + \mathbf{f}_1, \tag{20a}$$

$$A\mathbf{v}^{n+1} + 3B_y\,\mathbf{p}^n = -(A+E)\,\mathbf{v}^n + B_y\,\mathbf{p}^{n-1} + \mathbf{f}_2, \tag{20b}$$

$$A\mathbf{w}^{n+1} + 3C_2\,\mathbf{p}^n = -(A+E)\,\mathbf{w}^n + C_2\,\mathbf{p}^{n-1} + \mathbf{f}_3, \tag{20c}$$

$$B_x\,\mathbf{u}^{n+1} + B_y\,\mathbf{v}^{n+1} + C_1\,\mathbf{w}^{n+1} = 0. \tag{20d}$$

where A, B_x, B_y, C_1, C_2 are $NZ-2 \times NZ-2$ matrices, $\mathbf{u} = (\tilde{u}_1, \tilde{u}_2, \ldots, \tilde{u}_{NZ-2})^t$, and $\mathbf{f}_1 = (\tilde{d}_{1,1}, \tilde{d}_{1,2}, \ldots, \tilde{d}_{1,NZ-2})^t$, etc. Here, A represents the operator $\{-\nu'_e(k'^2_x + k'^2_y) - 2/\Delta t + \nu'_e\,\partial^2/\partial z^2\}$, $B_x = -\sqrt{-1}\,k'_x I$, $B_y = -\sqrt{-1}\,k'_y I$, C_1 and C_2 represent $-\partial/\partial z$, $E = 4I/\Delta t$, I is a unit matrix, $\sqrt{-1}$ is the imaginary unit, and ν'_e denotes $\langle \nu_e \rangle^n + 1/\mathrm{Re}$. These difference equations are closed as follows: the velocity components are set to zero on the walls, and a numerical boundary condition for the pressure on the walls is imposed. This boundary condition is given so as to fulfill the continuity of normal momentum across the wall, by using the z component of (16) on the wall. Namely,

$$\frac{2}{\mathrm{Re}}\left(\frac{w_{-1}^{n+1}}{(h_1+h_0)\,h_0} - \frac{w_0^{n+1}}{h_1 h_0} + \frac{w_{-1}^{n+1}}{(h_1+h_0)\,h_1}\right) - 3\frac{p_1^n - p_{-1}^n}{h_1+h_0}$$
$$= -\frac{2}{\mathrm{Re}}\left(\frac{w_{-1}^n}{(h_1+h_0)\,h_0} - \frac{w_0^n}{h_1 h_0} + \frac{w_1^n}{(h_1+h_0)\,h_1}\right) - \frac{p_1^{n-1} - p_{-1}^{n-1}}{h_1+h_0}. \tag{21}$$

where w_{-1} and p_{-1} denote the values of w and p at external fictitious grid point z_{-1}, respectively. w_0 is set to zero from a no-slip condition at the wall, and w_{-1} is set equal to w_1 from the difference form of the continuity equation. Equation (21), however, is not sufficient to close Eq. (20c) and an extra boundary condition for pressure is imposed: p_{-1} is extrapolated with second-order polynomial using the values of p_0, p_1, p_2 to retain the second-order accuracy. Similar conditions are imposed at the upper wall. These boundary conditions are incorporated into C_2.

Here, let us show the reason why the Adams–Bashforth method is applied to the pressure gradient terms. In Type II, the Poisson-like equation for the pressure can be derived as

$$3D\,\mathbf{p}^n = D\,\mathbf{p}^{n-1} - B_x(I + A^{-1}E)\,\mathbf{u}^n - B_y(I + A^{-1}E)\,\mathbf{v}^n$$
$$- C_1(I + A^{-1}E)\,\mathbf{w}^n + B_x A^{-1}\,\mathbf{f}_1 + B_y A^{-1}\,\mathbf{f}_2 + C_1 A^{-1}\,\mathbf{f}_3, \tag{22}$$

where

$$D = -(k'^2_x + k'^2_y)\,A^{-1} + C_1 A^{-1} C_2.$$

Note that Eq. (22) is obtained through Gauss elimination of $\mathbf{u}^{n+1}$, $\mathbf{v}^{n+1}$, $\mathbf{w}^{n+1}$ from (20), which has already been closed by imposing boundary conditions. Therefore, no additional boundary condition is required. (22) can be written in the form that

$$(-k'^2_x I - k'^2_y I + AC_1 A^{-1} C_2)\,\mathbf{p}^n = \mathrm{RHS}. \tag{23}$$

By solving Eq. (22), $\mathbf{p}^n$ is obtained, and we get $\mathbf{u}^{n+1}$, $\mathbf{v}^{n+1}$, and $\mathbf{w}^{n+1}$ by inserting $\mathbf{p}^n$ to Eqs. (20a), (20b), and (20c).

Equation (22) becomes

$$\mathbf{p}^{n+1} = -\mathbf{p}^n + \mathbf{S}^n \tag{24a}$$

for the Crank–Nicolson method and

$$\mathbf{p}^n = \tfrac{1}{3}\,\mathbf{p}^{n-1} + \mathbf{S}^n \tag{24b}$$

for the Adams–Bashforth method, where $\mathbf{S}^n$ denotes the source term. The solution of difference equations (24a and 24b) are given as (25a and 25b), respectively:

$$\mathbf{p}^n = (-1)^n\,\mathbf{p}^0 + \sum_{j=0}^{n-1} (-1)^{n-j-1}\,\mathbf{S}^j, \tag{25a}$$

$$\mathbf{p}^n = \left(\frac{1}{3}\right)^n \mathbf{p}^0 + \sum_{j=1}^{n} \left(\frac{1}{3}\right)^{n-j} \mathbf{S}^j. \tag{25b}$$

Therefore, oscillatory solutions in time can occur in the Crank–Nicolson method. To confirm this point, the decay of fluctuations was computed at low Reynolds numbers ($\mathrm{Re} \sim 10$): velocity fluctuations decayed, whereas pressure exhibited both timewise and meshwise oscillations. Therefore the instantaneous pressure distribution is not reliable by the Crank–Nicolson method unless we average $\bar{p}^n$ and $\bar{p}^{n+1}$. On the other hand, this problem is resolved by the Adams–Bashforth method.

In the conventional scheme of MAC type [19], if the viscous terms are treated implicitly, Eqs. (20a), (20b), and (20c) are multiplied by B_x, B_y, C_1, respectively. Assuming that A and C_1 commute and using (20d), the Poisson equation for the pressure $\mathbf{p}$ becomes:

$$(-k_x'^2 I - k_y'^2 I + C_1 C_2)\,\mathbf{p} = \mathrm{RHS}, \tag{25}$$

where $C_1 C_2$ approximates $\partial^2/\partial z^2$. For the nonuniform grids, because A and C_1 do not commute, the discrete operators in the Poisson equation (25) are not consistent with the discrete operators applied to the Navier–Stokes and continuity equations. In the present method, however, they are constructed consistently. This is one of the advantages of the present method.

For $k_x' = k_y' = 0$, $\mathbf{w}$ is set to zero from Eq. (20d), $\mathbf{u}$ and $\mathbf{v}$ are determined from Eqs. (20a) and (20b), respectively, and $\mathbf{p}$ is given by setting $\tilde{p}_0 = 0$ and then solving (20c) succesively in the z direction.

Types I and II differ in efficiency, although they are equivalent mathematically. In Type I, if Eqs. (19) are ordered as $\bar{u}$ momentum, $\bar{v}$ momentum, $\bar{w}$ momentum, and continuity, the diagonal block has a zero diagonal element, which may seriously degrade the computation. This problem is removed by ordering the equations: continuity, $\bar{v}$ momentum, $\bar{w}$ momentum, and $\bar{u}$ momentum, but dominance of diagonal elements is not guaranteed. This problem is absent in Type II [11]. However, the

coefficient matrix D of (22) is full. Thus direct solution of (22) by Gauss elimination would require $O((NZ-2)^3)$ arithmetic operations at each time step. All the results shown in the present paper are obtained with Type I.

3.2. *Estimate of Truncation Errors Involved in the Arakawa and Rotational Forms*

In this study, two forms of the convective terms in the Navier–Stokes equations are used. One is the Arakawa form, and the other is the rotational form. In [11], the Arakawa form

$$\frac{1}{2}\left\{\frac{\delta}{\delta x_j}(\bar{u}_i\bar{u}_j)+\bar{u}_j\frac{\delta\bar{u}_i}{\delta x_j}+\bar{u}_i\frac{\delta\bar{u}_j}{\delta x_j}\right\} \tag{26}$$

was employed following [17] ($\delta/\delta x_j$ denotes a second-order central difference in the j direction). The Arakawa form was found to work quite well. We extended the method of [17] to allow a no-slip boundary condition on the walls. In the present study, the partial differential operators in the x and y directions are estimated by the pseudo-spectral method. On the other hand, the rotational form of the convective terms can be written

$$\bar{u}_j\left(\frac{\partial\bar{u}_i}{\partial x_j}-\frac{\partial\bar{u}_j}{\partial x_i}\right)+\frac{1}{2}\frac{\partial}{\partial x_i}(\bar{u}_j\bar{u}_j). \tag{27}$$

Both the Arakawa and rotational forms preserve mean momentum and energy in the discretized sense.

It is numerically revealed that the major error in the Arakawa form occurs in the x-momentum equation:

$$\frac{1}{2}\bar{w}\frac{\partial\bar{u}}{\partial z}+\frac{1}{2}\bar{u}\frac{\partial\bar{w}}{\partial z}+\frac{1}{2}\frac{\partial}{\partial z}(\bar{u}\bar{w}). \tag{28}$$

On the other hand, the major error in the rotational form comes from the terms

$$-\bar{u}\frac{\partial\bar{u}}{\partial z}+\frac{1}{2}\frac{\partial}{\partial z}\bar{u}^2 \tag{29}$$

in the z-momentum equation.

Equations (28) and (29) are approximated by

$$\frac{1}{2}\bar{w}_k\frac{\bar{u}_{k+1}-\bar{u}_{k-1}}{h_{k+1}+h_k}+\frac{1}{2}\bar{u}_k\frac{\bar{w}_{k+1}-\bar{w}_{k-1}}{h_{k+1}+h_k}+\frac{1}{2}\frac{\bar{u}_{k+1}\bar{w}_{k+1}-\bar{u}_{k-1}\bar{w}_{k-1}}{h_{k+1}+h_k} \tag{30}$$

and

$$-\bar{u}_k\frac{\bar{u}_{k+1}-\bar{u}_{k-1}}{h_{k+1}+h_k}+\frac{1}{2}\frac{\bar{u}_{k+1}^2-\bar{u}_{k-1}^2}{h_{k+1}+h_k}, \tag{31}$$

respectively. Using Taylor expansions around z_k, we get the error estimate for (31)

$$(h_{k+1}-h_k)\left(\frac{\partial \bar{u}}{\partial z}\right)^2. \tag{32}$$

The horizontal average of (32) can be written

$$(h_{k+1}-h_k)\left(\frac{\partial \langle \bar{u} \rangle}{\partial z}\right)^2 + (h_{k+1}-h_k)\left\langle\left(\frac{\partial \bar{u}''}{\partial z}\right)^2\right\rangle. \tag{33}$$

Because $\langle \bar{u} \rangle$ is linear in z_+ near the walls, the first term in (33) becomes $(h_{k+1}-h_k)\,\mathrm{Re}^2$. Further, $(h_{k+1}-h_k)$ can be estimated as

$$(h_{k+1}-h_k) \sim (\Delta\xi)^2\,\chi(\xi), \tag{34}$$

where

$$\chi(\xi)=\frac{\partial^2 z}{\partial \xi^2}= -c_0^2\frac{\tanh(c_0\xi)}{\alpha\cosh^2(c_0\xi)}.$$

Hence, the first term in (33) is approximately $(\Delta\xi)^2\,\chi(1)\,\mathrm{Re}^2$. This is of order 10^2 to 10^3 in the current computation and introduces a large error into (20c) near the wall.

The corresponding truncation error for (30) is estimated to be

$$(h_{k+1}-h_k)\left\langle \frac{\partial \bar{u}}{\partial z}\frac{\partial \bar{w}}{\partial z} + \bar{u}\frac{\partial^2 \bar{w}}{\partial z^2} + \bar{w}\frac{\partial^2 \bar{u}}{\partial z^2}\right\rangle. \tag{35}$$

The limiting slope of the normal velocity at the wall is zero. Therefore, with a no-slip boundary condition at the wall, the error (35) is smaller than (33) by the order of 10^3 to 10^4. Thus, no serious error is introduced by using the Arakawa form (26).

The governing equation for the balance of the GS portion of turbulent energy (12) can be derived by multiplying (5) by $\bar{u}_i''$ and averaging horizontally. If the rotational form is used, the production term arises from the term $\bar{u}_i''\,\partial(\bar{u}_j\bar{u}_j)/\partial x_i$. In some formulations, the total GS energy $\bar{u}_j\bar{u}_j/2$ is added to the pressure and treated as the pressure head. In that case, if proper care is not taken in the approximation of the pressure-gradient terms, the production of turbulent energy may be incorrect. Splitting the velocity components to the mean streamwise velocity and the deviation part i.e. $\bar{u}_i = \langle \bar{u}_i \rangle\,\delta_{i1} + \bar{u}_i''$, is recommended. Inserting this expression in the convective terms we get

$$\bar{u}_j\frac{\partial \bar{u}_i}{\partial x_j} = \langle \bar{u}_1 \rangle\frac{\partial \bar{u}_i''}{\partial x} + \bar{w}\frac{\partial \langle \bar{u}_i \rangle}{\partial z}\,\delta_{i1} + \bar{u}_j''\frac{\partial \bar{u}_i''}{\partial x_j}. \tag{36}$$

If the last term in the right-hand side of (36) is treated by the rotational form, the

first term in the error estimate (33) is eliminated. It is considered that this splitting of velocity is related to the residual stress model, because in both the mean part is separated and explicitly used in the computation.

3.3. *Computed Cases*

The region to be treated has a streamwise length (L_x) of 3.2 H or 4.8 H and a spanwise one (L_y) of 1.6 H. The size of computational domain in the x and y directions must minimize the effect of the imposed periodic boundary conditions. The two-point correlation measurements of [20] are used as a criterion. Re is chosen as 1280 ($R_c = 27800$).

The initial condition was generated by interpolating the data obtained in the previous computation [4] with $32 \times 32 \times 32$ grid points. Computations were done until a statistically steady state was reached and continued to obtain reliable statistical quantities. In all cases shown here, the time interval Δt is 0.0005.

The Arakawa form is employed in Case 1. The nondimensional integration time of Case 1 is 9.85. The rotational form is used in Case 2. This computation was restarted from an intermediate stage of Case 1 (at $t = 9.6$), and the convective terms are switched from the Arakawa form to the rotational form and extended until $t = 11.1$. Case 3 is restarted from $t = 9.6$ of Case 1: L_x is increased to 4.8 to check the dependence on the size of computational box and extended until $t = 12.6$. Ensemble averages are obtained from the last 3.0 and 1.5 time units in Case 1 and in Cases 2 and 3, respectively. In Sections 4 and 5, $\langle \cdot \rangle$ indicates horizontal-time averaged values.

A regular grid system was used. Results with a staggered grid system and the rotational form have been omitted, where the residual stress model was not employed. They showed no significant differences from Case 2 of the present study.

All computations were done with the HITAC S-810 Model 20 system of the Computer Center of the University of Tokyo. The main memory was 2 million 64-bit words and we utilized 4.5 million words of extended storage (ES), which is composed of semiconductor memory. Use of ES instead of the magnetic disk, remarkably reduced I/O wait time. The computer time, including I/O time, is 6.5 s per time step. The computed cases are summarized in Table I.

TABLE I

Case Specifications, Grid Parameters, the Size of Computational Domain, Forms of Approximation for the Convective Terms in the Navier–Stokes Equations

Case	NX	NY	NZ	L_x	L_y	Convective terms
1	64	64	62	3.2	1.6	Arakawa
2	64	64	62	3.2	1.6	Rotational
3	64	64	62	4.8	1.6	Arakawa

Features of the boundary layer flow in the near wall region were revealed by Kline *et al.* [21]. They found an array of high- and low-speed regions called "streaks." The mean spacing of the streaks is approximately 100 wall units.

4. Results and Discussion of Case 1

In this section, we show the results from Case 1 and compare with previous numerical simulations [1 and 2]. In [1], spectral methods were used in the x-direction with $NX=64$, in the y-direction with $NY=128$, and finite differences were used in the z-direction with $NZ=63$. In the present study, $NX=NY=64$ and $NZ=62$. In [2], $NX=NY=128$ with 65 Chebyshev polynomials expansion in the z-direction.

Figure 1 shows the mean streamwise velocity profile. This profile is fit by $\langle \bar{u} \rangle = z_+$ in the vicinity of the wall and in the logarithmic region approximately

$$\langle \bar{u} \rangle = (1/0.4) \log z_+ + 6.2. \tag{37}$$

The Karman constant obtained (0.4) is in good agreement with the value determined experimentally in [22, 23], but the constant $B=6.2$ is larger than the generally accepted value of 5.0 in [23, 24], and that in [1], and close to the value of 5.9 in [25]. However, the value is considerably improved from 7.0 in the computation with $32\times32\times32$ grid points [4]. This constant seems to be controllable by the constant c^* in the residual stress model (11). In the present study, we abandoned the residual stress model and cannot control B.

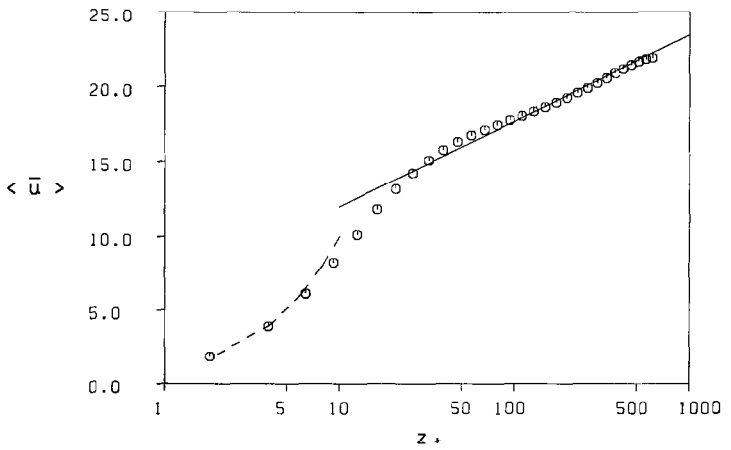

FIG 1. Mean streamwise velocity profile $\langle \bar{u} \rangle$ from Case 1; ○, computation; ———, $\langle \bar{u} \rangle = z_+$; ———, $\langle \bar{u} \rangle = 1/0.4 \log z_+ + 6.2$.

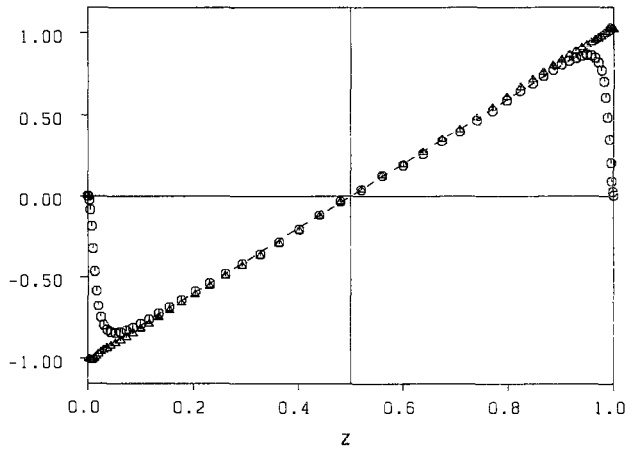

FIG. 2 Mean GS Reynolds stress and the total stress from Case 1; ○, $\langle \bar{u}''\bar{w} \rangle$; —, $\langle \bar{u}''\bar{w} \rangle - \langle \nu_e (\partial\bar{u}/\partial z + \partial\bar{w}/\partial x) \rangle - (1/\mathrm{Re})(\partial\langle \bar{u} \rangle/\partial z)$.

Figure 2 plots the profiles of the GS mean Reynolds stress $\langle \bar{u}''\bar{w} \rangle$ and the total stress

$$\langle \bar{u}''\bar{w} \rangle - \left\langle \nu_e \left(\frac{\partial \bar{u}}{\partial z} + \frac{\partial \bar{w}}{\partial x} \right) \right\rangle - \frac{1}{\mathrm{Re}} \frac{\partial \langle \bar{u} \rangle}{\partial z}.$$

The total stress balances the mean pressure gradient, indicated by a dashed line in the figure. The computation appears to be in statistical equilibrium.

Figure 3 shows the profiles of the correlation function between the GS streamwise and normal components of the fluctuations,

$$\langle u''\bar{w} \rangle / \langle \bar{u}''^2 \rangle^{1/2} / \langle \bar{w}^2 \rangle^{1/2}.$$

The profiles agree fairly well with the data of [26].

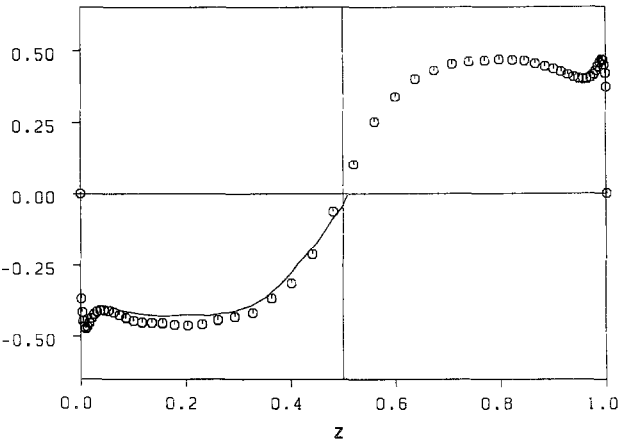

FIG. 3 Correlation coefficient between the GS streamwise and normal components of fluctuations from Case 1 (○); ———, experimental data in [26].

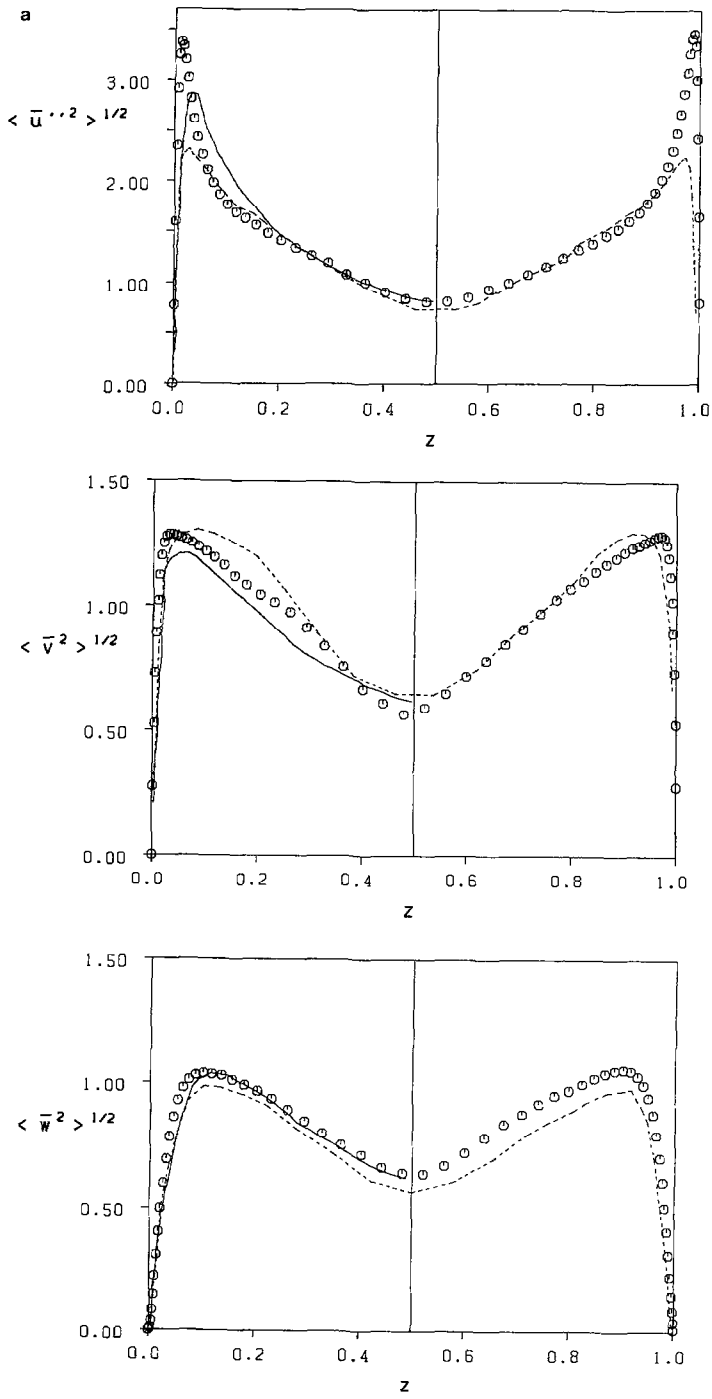

FIG. 4. (a) GS turbulence intensities from Case 1 (○); ———, computational data in [1]; ———, experimental data in [27]. (b) GS turbulence intensities in the vicinity of the lower wall from Case 1 (○); ———, computational data in [1].

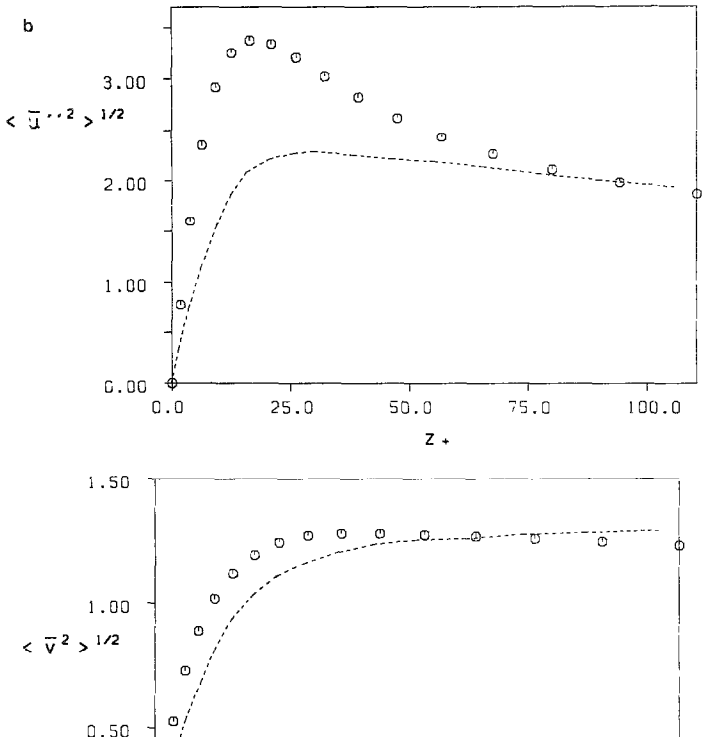
b
3.00
2.00
1.00
0.00
0.0
25.0
50.0
75.0
100.0
Z +
1.50
1.00
0.50

Figure 4a displays GS turbulence intensities in the x, y, z directions and Fig. 4b shows the intensities in the vicinity of the lower wall in wall units. For comparison, the computational data of [1] and the experimental measurement in [27] are shown. From these figures, we see that the amplitude of $\langle \bar{u}''^2 \rangle^{1/2}$ is larger than in [1, 27] and $\langle \bar{w}^2 \rangle^{1/2}$ is slightly larger than in [1, 27]. We find an appreciable difference in $\langle \bar{v}^2 \rangle^{1/2}$ between the present result and that of [1]: the position of the peak is closer to the wall and shows better agreement with [27]. The overall agreement with [27] is good.

Figure 5 plots the streamwise two-point correlation function

$$R_{ii}(r_1; z) = \langle \bar{u}_i''(x + r_1, y, z)\, \bar{u}_i''(x, y, z) \rangle / \langle \bar{u}_i''^2(x, y, z) \rangle, \tag{38}$$

at two locations ($z = 0.0129$ and 0.0626). The profiles of R_{11} $(r_1; z)$ at $z = 0.055$ from [20] and $R_{11}(r_1; z)$ at $z = 0.0125$ and 0.0605 from [1] are included. The profiles are at slightly different vertical locations. As found in [1], for small values of r_1, the measured correlations in [20] are smaller than the computed results. For larger values of r_1, the computed results are smaller than experimental measurements in [20]. The present correlation persists over a longer distance in the downstream direction than in [1] and agrees with the experimental observation that mean streamwise length of streaks is greater than 1000 wall units [28]. To

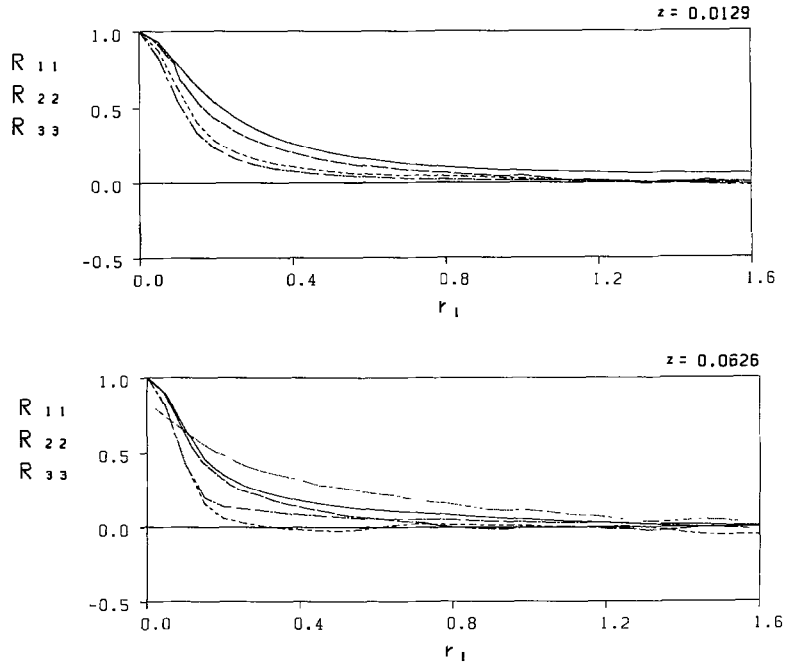

FIG. 5. Streamwise two point correlation function $R_{ii}(r_1; z)$; ———, R_{11} from Case 1 of the present study; – – –, R_{22}, — — — —, R_{33}; ···, experimental data in [20], ———, computational data in [1].

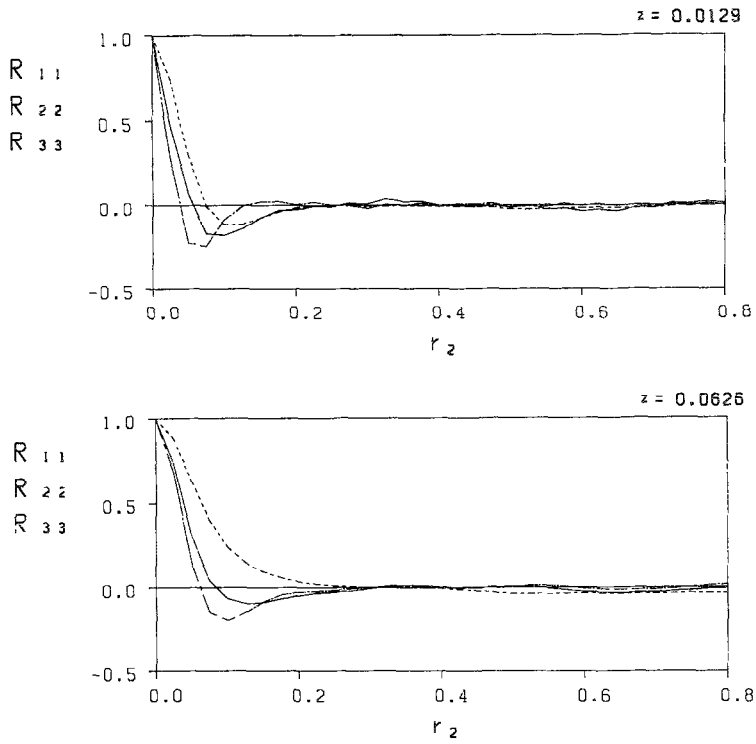

FIG 6. Spanwise two point correlation function $R_{ii}(r_2; z)$, ———, R_{11}; – – –, R_{22}; ———— , R_{33}.

check the dependence of streamwise correlations on the size of the computational box in the streamwise direction, L_x was elongated to 4.8 in Case 3. The results showed a tendency similar to Case 1.

The spanwise two-point correlation functions $R_{ii}(r_2; z)$ defined by

$$R_{ii}(r_2; z) = \langle \bar{u}_i''(x, y, z)\, \bar{u}_i''(x, y + r_2, z) \rangle / \langle \bar{u}_i''^2(x, y, z) \rangle, \tag{39}$$

at the same locations as in Fig. 5 are plotted in Fig. 6. Using the position of the first negative peak of $R_{11}(r_2; z)$, we can estimate the mean streak spacing as 250, which is considerably larger than the generally accepted value of 100 [21]. A similar defect is reported in [1]. The reason for this discrepancy may be, as pointed out in [1], that the grid resolution is not sufficient for the Reynolds number considered. Nevertheless, our mean spacing of streaks is found to be very close to that of [1], in spite of the fact that the number of grid points employed in the spanwise direction is half that in [1].

Figures 7a, b, and c display the budget of the GS portion of three components of turbulent intensities. In the downstream direction, the production and dissipation terms are dominant in the central region, but the diffusion term is dominant near the wall. The diffusion term changes from positive to negative as we depart from the

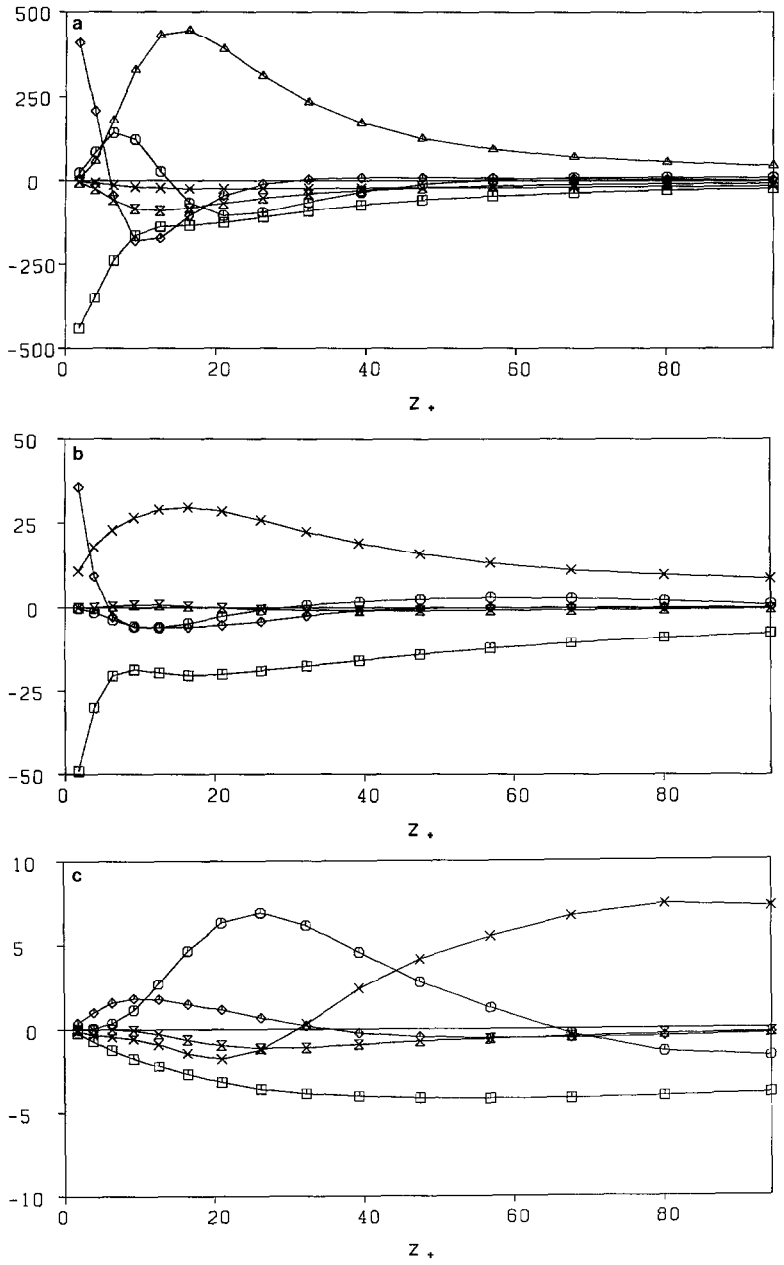

FIG. 7. (a) Balance of ensemble averaged GS portion of the streamwise component of turbulent kinetic energy from Case 1. △, production; ○, convection; ×, velocity–pressure gradient; ◇, diffusion; □, dissipation; ⧖, cascade. (b) Balance of GS portion of the spanwise component of turbulent kinetic energy. See caption of Fig. 7a for details. (c) Balance of GS portion of the normal component of turbulent kinetic energy. (d) Balance of GS portion of the normal component of turbulent kinetic energy from previous numerical calculations [1]. (e) Balance of GS portion of the normal component of turbulent kinetic energy in the vicinity of concave wall from previous numerical calculations [2]. Note that the positions of markers do not coincide with the Chebyshev collocation points.

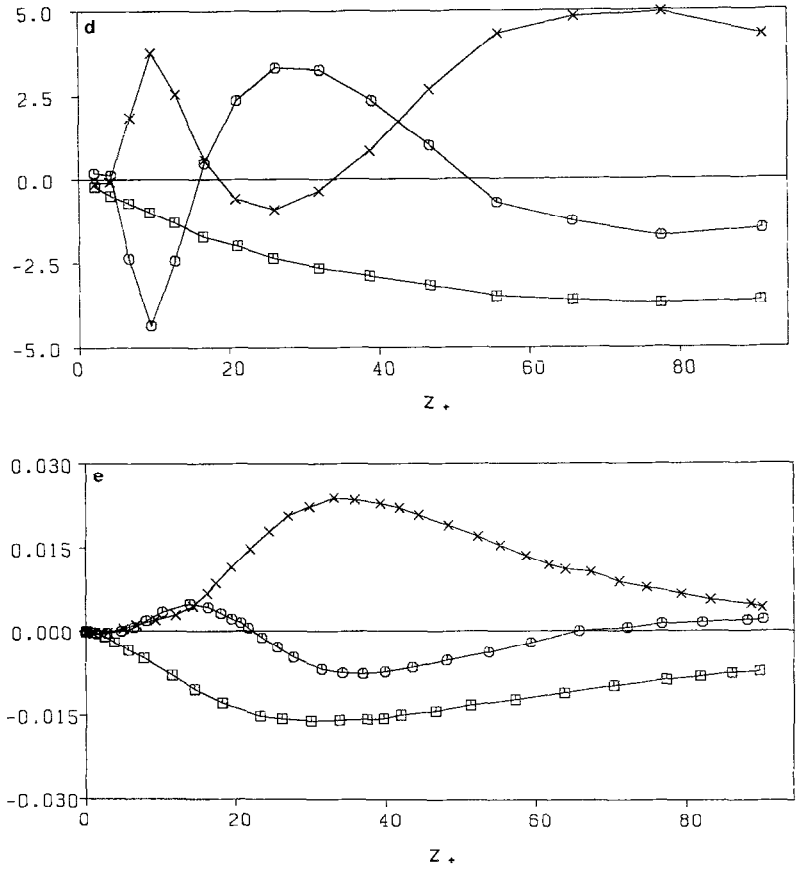

FIG. 7—*Continued.*

wall [4]. The balances in both the streamwise and spanwise components are qualitatively the same as in [1], but the peak values of the production and dissipation terms in the streamwise component are larger. However, the GS balance for $\langle \bar{w}^2 \rangle$ is qualitatively different from that of [1]. Partial results from [1] are reproduced in Fig. 7d. In both in [1] and the present study, the velocity–pressure gradient term balances the dissipation term in the central region. On the other hand, the velocity–pressure gradient term has a large gain, peaked at $z_+ \sim 10$ in [1]. The convection term makes up for this peak. This peak is absent in the present study. Figure 7e shows the corresponding energy balance from a direct simulation of a mildly curved channel flow [2]. Although the contribution of the convection term in the present study is larger than in [2], the qualitative agreement is good. The effect of curvature in [2] and the difference in the Reynolds number should be noted. For the former, in [2], computation was performed at a mild curvature. Therefore, the comparison with the present study will be plausible because

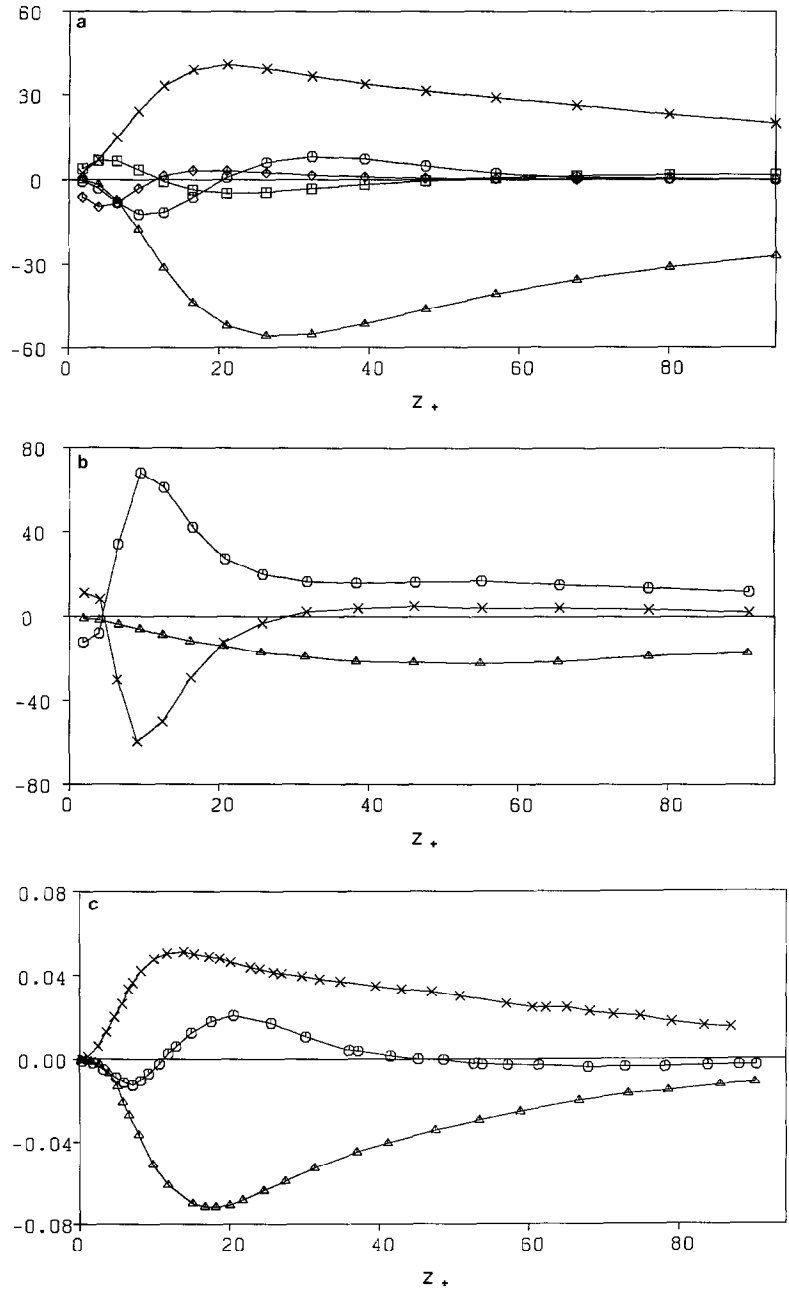

FIG. 8. (a) Balance of ensemble averaged GS portion of turbulent shear stress from Case 1. See caption of Fig. 7a for details. (b) Balance of GS portion of turbulent shear stress from previous numerical calculations [1]. (c) Balance of GS portion of turbulent shear stress in the vicinity of concave wall in previous numerical calculations [2]. See captions of Figs. 7a and 7e for details.

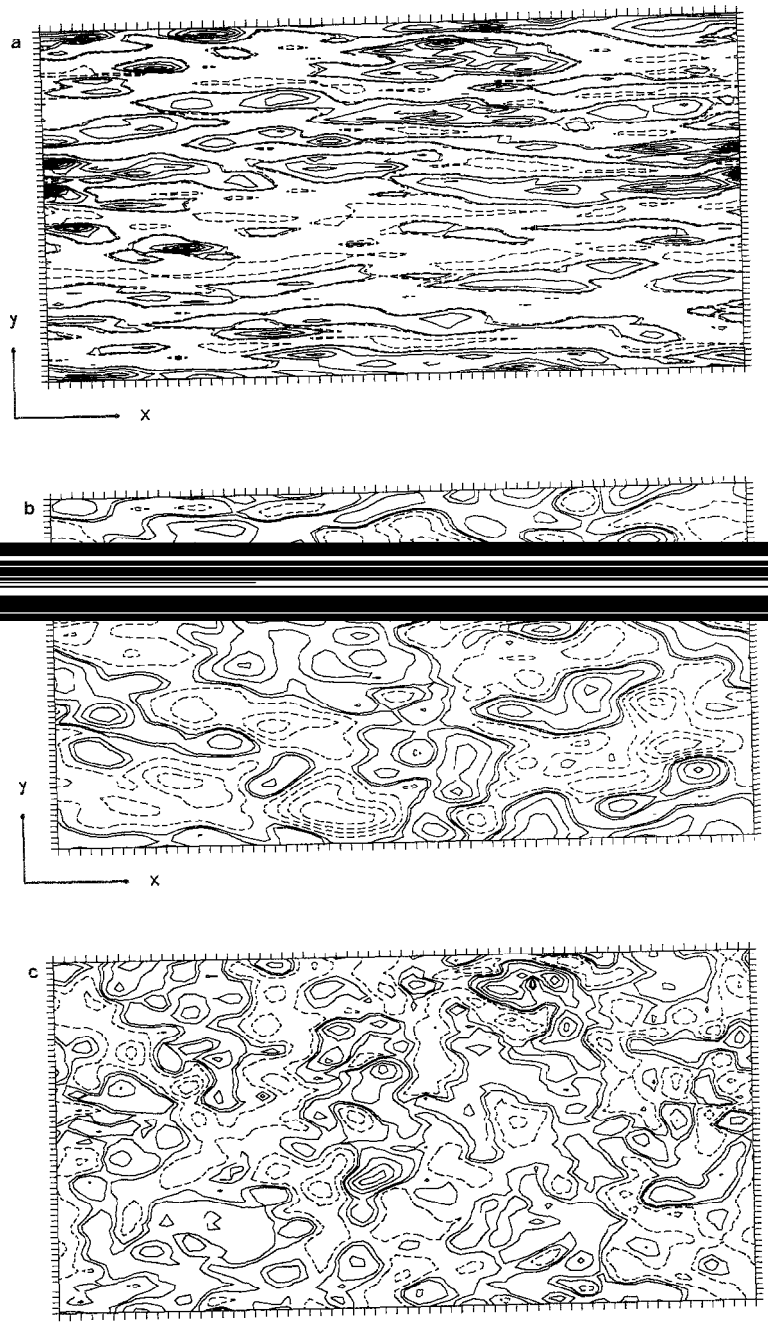

FIG. 9 (a) Contour lines of $\bar{u}''$ in the x–y plane at $z_+ = 6.4$, $t = 9.6$ from Case 1. (b) Contour lines of $\bar{u}''$ in the x–y plane at $z_+ = 614$, $t = 9.6$ from Case 1 (c) Contour lines of $\bar{p}''$ in the x–y plane at $z_+ = 6.4$, $t = 9.6$ from Case 1.

the curvature will not affect the results crucially until z_+ is sufficiently large [2]. The Reynolds number in [2] is 336 compared with 1280 in [1]. The large peak of the velocity–pressure gradient term in the vicinity of the wall in [1] may be due to the higher Reynolds number.

A greater difference is seen in the balance of the GS portion of turbulent shear stress. Figures 8a, b, and c display the budget of the GS portion of turbulent shear stress in the present study, [1], and [2], respectively (only production, convection, and velocity–pressure gradient terms are reproduced in Figs. 8b and 8c). Large peaks in both the convection and the velocity–pressure gradient terms are found in [1], whereas these peaks are absent in the present study and [2]. Instead, the production term has a large peak at $z_+ \sim 25$ in the present study and at $z_+ \sim 15$ in [2]. (The difference in the position of peak suggests insufficiency of the number of grid points employed in the present study.) In the central region of the channel, the convection term balances the production term in [1], whereas the velocity–pressure gradient term balances the production term in both the present study and [2]. This discrepancy is important for modeling. No experimental arguments of the budget of turbulent shear stress are available, but the large peak in the production term near the wall is consistent with the experimental observation that the turbulent energy production is maximum at $z_+ \sim 15$ (see [29]).

Figure 9a plots the instantaneous contour lines of $\bar{u}''$ in the x–y plane located at $z_+ = 6.4$ at $t = 9.6$. Positive values are contoured by solid lines and negative values by dashed lines. Highly elongated regions of high- and low-speed fluid $\bar{u}''$, which correspond to the experimentally observed streaks, can be discerned. However, the mean spacing of streaks is approximately 250 wall units. The instantaneous contour lines of $\bar{u}''$ in the x–y plane located at $z_+ = 614$ and at $t = 9.6$ is displayed in Fig. 9b. The streaky structures observed in Fig. 9a are absent. This agrees with the experimental observations in [21]. The instantaneous contour lines of $\bar{p}''$ in the x–y

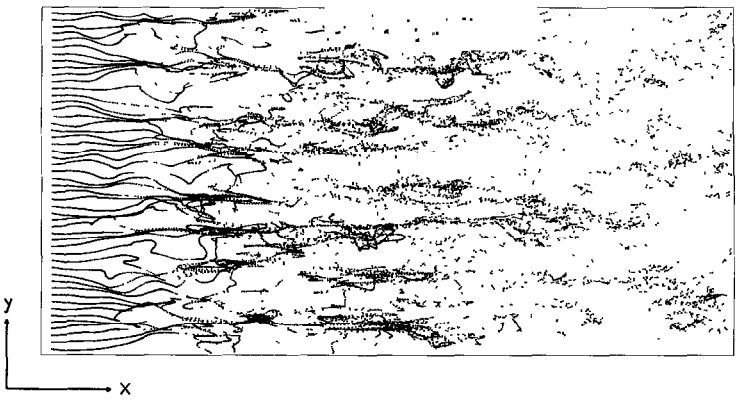

FIG. 10 Top view of streaky structure visualized by passive markers introduced along a horizontal wire set at $z_+ = 12.8$ from Case 1.

plane located at $z_+ = 6.4$ and at $t = 9.6$ are displayed in Fig. 9c. With the Adams–Bashforth method for pressure gradient terms, the meshwise oscillations are suppressed as shown in the figure, and the root mean square value of the GS wall pressure fluctuations is about 2.0, which is in fair agreement with the experimental measurement of 2.3 in [30] and the computational result 2.05 in [1].

Time lines from Case 1 are displayed in Fig. 10, where a wire is set parallel to the y-axis at $z_+ = 12.8$. The streaks can be clearly identified in this figure and agreement with experimental observations in [21] is good as in [1].

5. Results and Discussion of Case 2

In Case 2, the convective terms are switched from the Arakawa form to the rotational form. The mean streamwise velocity profile, the Reynolds stress distribution, and GS turbulence intensity of the streamwise component are plotted in Figs. 11, 12 and 13, respectively. The GS Reynolds stress and turbulence intensities decays. Thus the mean streamwise velocity profile returns to the laminar profile. Therefore, unless a residual stress model is used with the rotational form, the turbulence dies out. It is found that when the Arakawa form is switched to the rotational form, the large truncation error in the vicinity of the wall induces the spurious pressure. As a result, the velocity–pressure gradient term in the normal component of turbulent energy balance increases substantially. Thus, $\langle \bar{w}^2 \rangle^{1/2}$ appreciably increases. Because the approximation preserves mean energy, a transfer of turbulent energy from the downstream component to the spanwise and normal components arises: $\langle \bar{u}''^2 \rangle^{1/2}$ substantially decreases and $\langle \bar{v}^2 \rangle^{1/2}$ slightly increases.

Figure 14 shows the balance of the turbulent shear stress. Comparison with Fig. 8a reveals that the velocity–pressure gradient term changes sign from positive

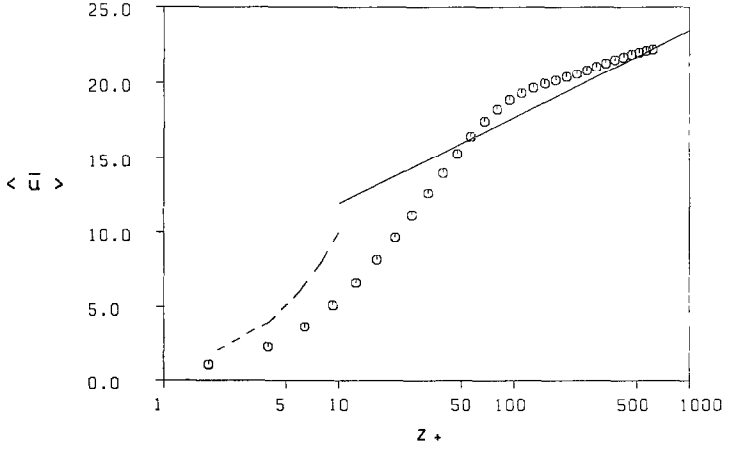

Fig. 11. Mean streamwise velocity profile $\langle \bar{u} \rangle$ from Case 2. See caption of Fig. 1 for details.

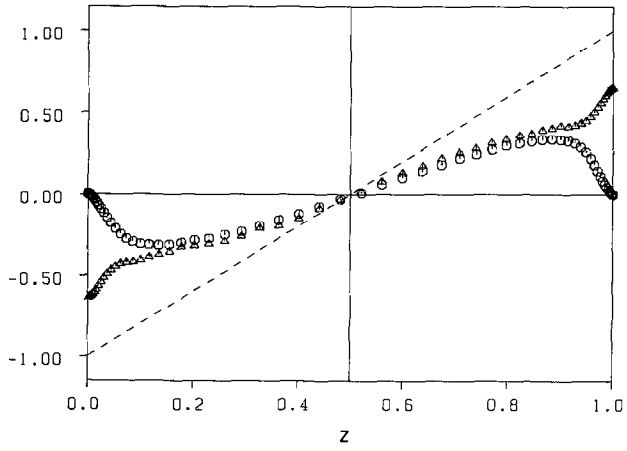

FIG. 12. Mean GS Reynolds stress and the total stress from Case 2; ○, $\langle \bar{u}''\bar{w}'' \rangle$; △, the total stress.

to negative. This change occurs immediately after we switch from the Arakawa form to the rotational form. The sum of all terms in the right-hand side of (13) is negative in the lower half of the channel. Thus the turbulent shear stress decreases in time. GS Reynolds stress and the correlation coefficient between the GS streamwise and normal components of fluctuations in the vicinity of the lower wall are plotted in Figs. 15 and 16, respectively. In Case 2, the GS Reynolds stress slightly increases in the amplitude at $z_+ \geqslant 10$, and changes sign from negative to positive at $z_+ \sim 2$ as in Fig. 16. The strong negative correlation coefficient at $z_+ \sim 10$ in Case 1 is absent at $t = 9.601$ in Case 2. Thus, the GS shear stress decays. The large peak in the production term observed in Fig. 8a disappears and is totally

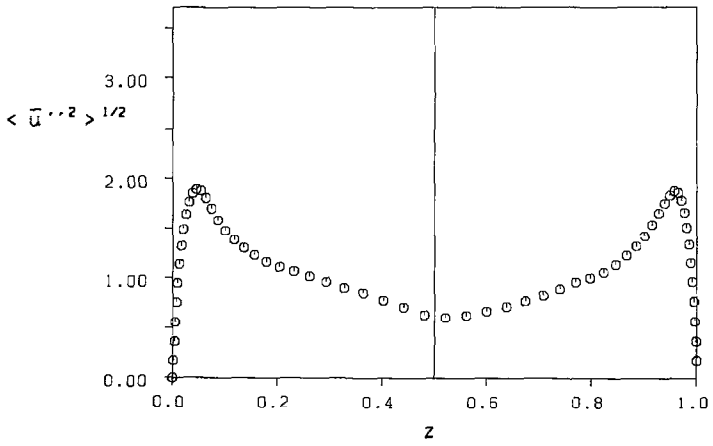

FIG. 13. GS turbulence intensities of streamwise component from Case 2 (○).

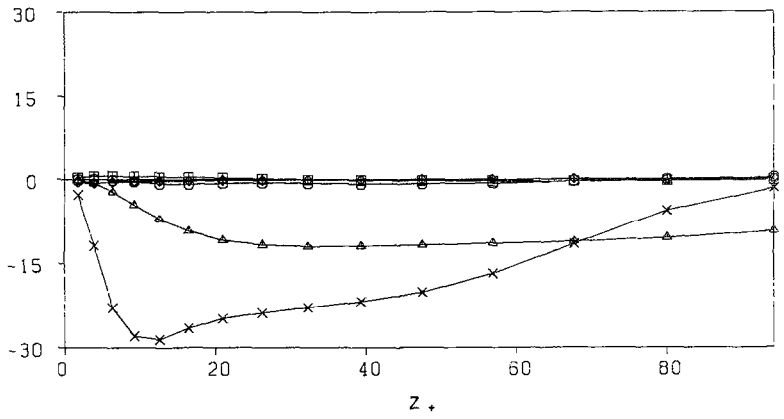

FIG 14. Balance of ensemble averaged GS portion of turbulent shear stress from Case 2 See caption of Fig. 7a for details.

absent from Fig. 14. The distributions of velocity–pressure gradient and production terms from Case 2 qualitatively agree with those in [1]. If we employ the residual stress model with the rotational form, the convection term will compensate for the velocity–pressure gradient term as in [1].

Finally, we compare Cases 1 and 2 from the viewpoint of helicity. The histograms of the probability density for the distribution of the angle θ between the fluctuating velocity $\zeta = (\bar{u}'', \bar{v}, \bar{w})'$ and vorticity $\boldsymbol{\omega}$ in the x–y plane at $z_+ = 1.8$, $t = 9.6$, are plotted in Fig. 17a. Here, $\boldsymbol{\omega}$ denotes $(\omega_1, \omega_2, \omega_3)'$, where $\omega_i = \varepsilon_{ijm}\, \partial \bar{u}''_m / \partial x_j$ and ε_{ijm} denotes the alternating tensor. The range $\cos\theta = -1$ to 1 is divided into 30 equally

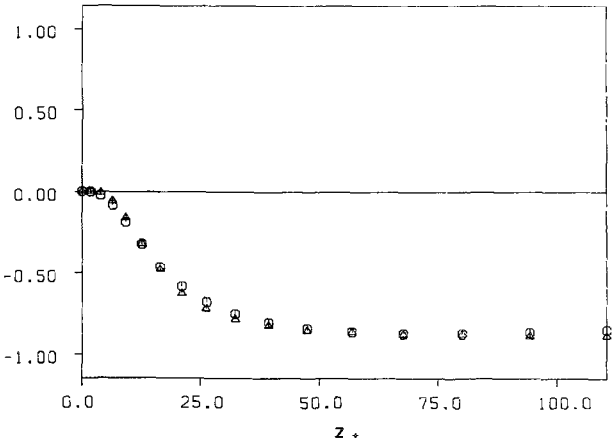

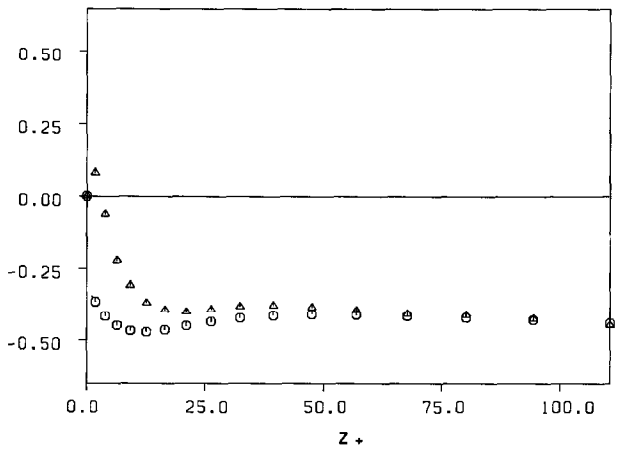

FIG. 16. Correlation coefficient between the GS streamwise and normal components of fluctuations: ○, from Fig. 3; △, at $t = 9.601$ from Case 2.

spaced intervals. The total number of data is 4096. Other samples (or different times) gave the same mean result. A sharp peak appears near $\cos\theta = 0$. Therefore, in the near wall region, the velocity vector is perpendicular to the vorticity vector. The weak helicity $(\zeta \cdot \omega)$ maximizes the absolute value of $\zeta \times \omega$ and results in the strong production of vorticity. Consequently, the production of turbulent energy is large. The correlation between the weak helicity and the strong production has been pointed out in plane channel and Taylor–Green vortex flows [31]. The distribution in Case 2 right after the Arakawa form is switched to the rotational form is plotted in Fig. 17b. Unlike in Case 1, the sharp peak in Fig. 17a is reduced. Thus, the production of turbulent energy is weakened. This is consistent with the absence of the peak in the production term of the GS portion of turbulent shear stress balance in Fig. 14. It is interesting to note that at $t = 11.1$ in Case 2, we switched back to the Arakawa form, and the turbulence began to revive.

6. CONCLUSIONS

Turbulent plane channel flow has been numerically studied using large eddy simulation, with the pseudo-spectral method in the downstream and spanwise directions and the second-order central finite differences in the normal direction. The numerical method is basically the same as in [1], but we have considered four choices in schemes for the convective terms and turbulence models. The convective term may be of either the Arakawa form (refered to as "CS" below) or the rotational form (RT) and the residual stress model may (RS) or may not (NORS) be employed. In [1], RT–RS was employed, and in Case 1 of the present study, CS–NORS is used. The difference in the balance of the grid scale portion of the tur-

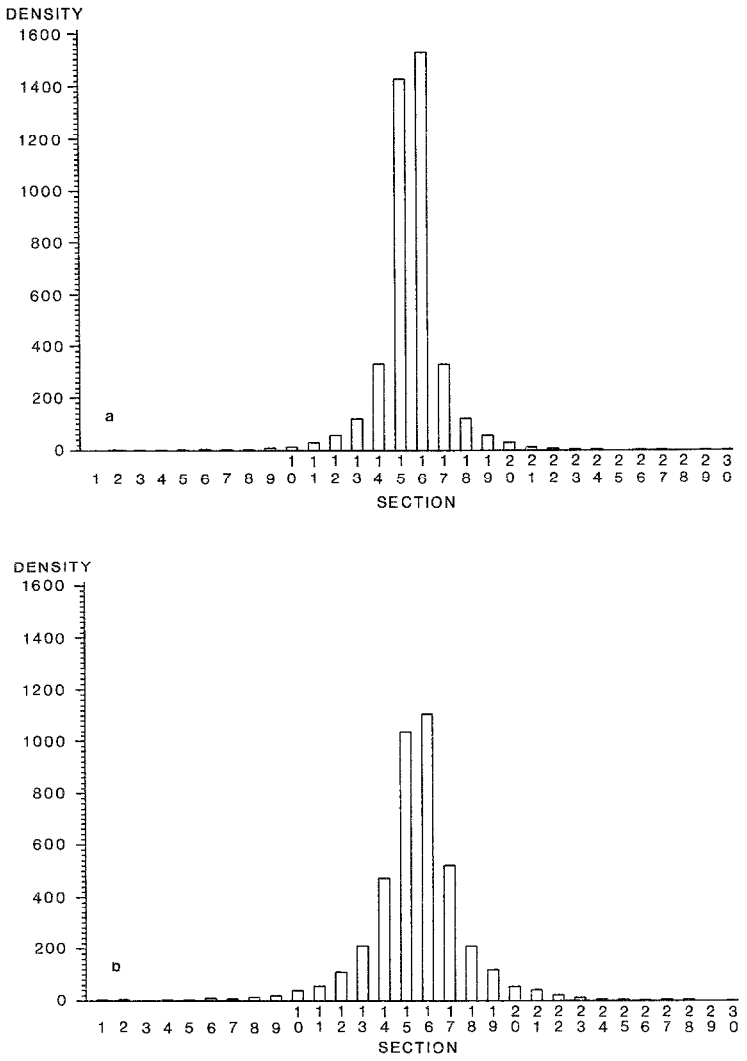

FIG. 17. (a) Histograms of $\cos\theta$ vs the probability density in the x–y plane at $z_+ = 1.8$, $t = 9.6$ from Case 1. (b) Histograms of $\cos\theta$ vs the probability density in the x–y plane at $z_+ = 1.8$, from Case 2, right after the Arakawa form is switched to the rotational form

bulent shear stress between the two cases is considerable. Appreciable differences are also found in turbulence intensities and two-point correlations. The mean spacing of streaks is 250 wall units, which is close to that in [1], although the number of grid points in the spanwise direction used here is half that in [1]. The results in the present study are qualitatively consistent with direct simulation [2]. An analytical estimate for the Arakawa and rotational forms shows the error to be large for the rotational form near the wall. This explains the poor results obtained

with this method. These errors may be absent when higher order schemes or Chebyshev polynomial expansions are used. However, the truncation error associated with the second-order central finite differences can lead to inaccurate results. Finally, we note that the CS–RS combination may improve the value of constant B in the logarithmic part of the mean streamwise velocity profile.

ACKNOWLEDGMENTS

The author is grateful to two referees for useful suggestions, most of which have been incorporated. The stimulating discussion with A. Yoshizawa is also appreciated.

REFERENCES

1. P. MOIN AND J. KIM, *J. Fluid Mech.* **118**, 341 (1982).
2. R D. MOSER AND P MOIN, NASA Technical Memorandum No. 85974, 1984 (unpublished).
3. A. WRAY AND M. Y HUSSAINI, AIAA Paper No. 80–0275, 1980 (unpublished).
4. K. HORIUTI, *J. Phys. Soc. Japan* **54**, 2855 (1985).
5. S. A. ORSZAG AND L. C KELLS, *J. Fluid Mech.* **96**, 159 (1980).
6. L. KLEISER AND U SCHUMANN, in *Proceedings of the Third GAMM Conference on Numerical Method in Fluid Mechanics, Cologne, West Germany*, 1979, edited by E. H. Hirschel (Vieweg, Braunschweig, 1980), p. 165.
7. S. A. ORSZAG AND A. T. PATERA, *J. Fluid Mech.* **128**, 347 (1983).
8. N. A. PHILLIPS, *Quart. J. R. Meteorol. Soc.* **82**, 123 (1956).
9. A. ARAKAWA, *J. Comput. Phys.* **1**, 119 (1966).
10. D. O. GOTTLIEB AND S. A. ORSZAG, *Numerical Analysis of Spectral Methods: Theory and Applications*, NSF–CBMS Monograph No 26 (Soc. Indus. Appl. Math., Philadelphia, 1977).
11. K. HORIUTI, *Theor. Appl. Mech.* **31**, 407 (1982).
12 U SCHUMANN, *J. Comput. Phys.* **18**, 376 (1975)
13. A. LEONARD, *Adv. Geophys.* **18A**, 237 (1974).
14. J. SMAGORINSKY, S. MANABE, AND J. L. HOLLOWAY, *Mon Weather. Rev.* **93**, 727 (1965).
15. A. YOSHIZAWA, *Phys. Fluids* **25**, 1532 (1982).
16. A. YOSHIZAWA AND K. HORIUTI, *J. Phys. Soc. Japan* **54**, 2834 (1985).
17 J. W DEARDORFF, *J. Fluid Mech.* **41**, 453 (1970).
18 E R. VAN DRIEST, *J. Aeronaut. Sci.* **23**, 1007 (1956).
19. F. H HARLOW AND J. E. WELCH, *Phys. Fluids* **8**, 2182 (1965).
20. G. COMTE-BELLOT, thesis, University of Grenoble, 1963 (unpublished).
21. S. J. KLINE, W. C REYNOLDS, F A SCHRAUB, AND P. W. RUNSTADLER, *J. Fluid Mech.* **30**, 741 (1967).
22. P. S. KLEBANOFF, NACA Report No. 1247, 1955 (unpublished).
23. A. K. M F. HUSSAIN AND W. C. REYNOLDS, *J. Fluids Eng* **97**, 568 (1975).
24. H. TENNEKES AND J. L. LUMLEY, *A First Course in Turbulence* (MIT Press, Cambridge, MA 1972), p. 149.
25. H. ECKLEMANN, *J. Fluid Mech.* **65**, 439 (1974).
26 J. SABOT AND G. COMTE-BELLOT, *J. Fluid Mech.* **74**, 767 (1976).
27. H. KREPLIN AND M. ECKLEMANN, *Phys. Fluids* **22**, 1233 (1979).
28. R. F. BLACKWELDER AND H. ECKELMANN, *J. Fluid Mech* **94**, 577 (1979).
29. H. T. KIM, S. J KLINE, AND W. C. REYNOLDS, *J. Fluid Mech.* **50**, 133 (1971)
30. W W. WILLMARTH, *Annu. Rev. Fluid Mech.* **7**, 13 (1975).
31. R B. PELZ, V. YAKHOT, S. A. ORSZAG, L. SHTILMAN, AND E. LEVICH, *Phys. Rev. Lett.* **54**, 2505 (1985).